Research Paper

WACCM simulations: Decadal winter-to-spring climate impact on middle atmosphere and troposphere from medium energy electron precipitation

Sigmund Guttu [a,*], Yvan Orsolini [b], Frode Stordal [a], Varavut Limpasuvan [c], Daniel R. Marsh [d,e]

[a] *University of Oslo, Problemveien 7, 0315, Oslo, Norway*
[b] *Norwegian Institute for Air Research, Instituttveien 18, 2007, Kjeller, Norway*
[c] *Coastal Carolina University, 100 Chanticleer Dr E, Conway, SC, 29528, USA*
[d] *National Center for Atmospheric Research (NCAR), 1850 Table Mesa Dr, Boulder, CO, 80305, USA*
[e] *Faculty of Engineering and Physical Sciences, University of Leeds, Leeds, UK*

A B S T R A C T

Energetic particle precipitation is one of the main processes by which the sun influences atmospheric composition and structure. The polar middle atmosphere is chemically disturbed by the precipitation-induced production of nitric oxides (NO_x) and hydrogen oxides (HO_x) and the associated ozone (O_3) loss, but the importance for the dynamics is still debated. The role of precipitating medium energy electrons (MEEs), which are able to penetrate into the mesosphere, has received increased attention, but has only recently begun to be incorporated in chemistry-climate models. We use the NCAR Whole Atmosphere Community Climate Model (WACCM) to study the climate impact from MEE precipitation by performing two idealized ensemble experiments under pre-industrial conditions, with and without the MEE forcing, over the period of the solar cycle 23 (only full calendar years, 1997–2007). Each experiment includes 20 11-year ensemble members, total 220 years. Our results indicate a strong month-to-month variability in the dynamical response to MEE throughout the winter period. We find a strengthening of the polar vortex in the northern hemisphere during December, but the signal decays rapidly in the following months. The polar vortex strengthening is likely attributable to planetary wave reduction due to increased zonal symmetries in upper stratospheric ozone heating, initially triggered by MEE-induced NO_x advected into the sunlit regions. We also find a similar early winter polar vortex strengthening in the southern hemisphere during June. Changes in mean meridional circulation accompany these anomalous wave forcings, leading to dynamically-induced vertical temperature dipoles at high latitudes. The associated weakening of the stratospheric mean meridional circulation results in an upper stratospheric polar ozone deficit in early winter. This polar cap ozone deficit is strongest in the southern hemisphere and contributes to a polar vortex weakening in late winter, in concert with increased planetary wave forcing. In both hemispheres, the stratospheric polar vortex signal seems to migrate downwards into the troposphere and to the surface.

1. Introduction

Deciphering the evolution of past climate and predicting future climate requires a detailed understanding of the role of relevant climate forcings. The solar forcing is one of the fundamental contributors to natural climate variability and many studies have been devoted in quantifying its role on various time scales. The solar forcing comprises two main components, namely electromagnetic radiation and energetic particle precipitation (EPP), each involving several mechanisms and pathways to influence the atmosphere (see Gray et al., 2010; Lockwood,

2012, for reviews). Variations in total solar irradiance have been linked to a "bottom-up" mechanism, initiated by changes in the sea surface temperature, cloudiness and convection (e.g., van Loon, 2012). Variations in spectral irradiance over the 11-year solar cycle are thought to initiate a top-down mechanism, starting with ozone and temperature changes in the mid and low-latitude upper stratosphere, followed by downward migration of zonal-mean zonal wind anomalies at high-latitudes (e.g., Kodera and Kuroda, 2002).

The influence of EPP also involves several pathways but its overall climate impact is heavily debated (Matthes et al., 2017; Sinnhuber and

Funke, 2020). The fact that sporadic solar protons events (SPEs) cause enhancements in nitric oxide (NO_x) in the stratosphere followed by catalytic ozone destruction has been known for several decades (Matthes et al., 2017 and references therein) and included in climate model simulations in the recent decade (e.g., Jackman et al., 2009). Similarly, the importance of geomagnetic activity and EPP for the mesosphere-lower thermosphere (MLT) composition has been recognized since the early 1990's (Callis et al., 1991) and recent studies have documented such composition changes in satellite data (Damiani et al., 2016; Funke et al., 2014; Fytterer et al., 2015; Reddmann et al., 2010; Sinnhuber et al., 2018). With energy below 30 keV, auroral electrons penetrate to the mesopause region while, with higher energies (30 keV–1000 keV), the medium-to-high energy electrons (MEEs) originating from the radiation belts are able to reach the lower mesosphere. The quantification of the MEE impact on the atmosphere has been receiving increased attention. Although case studies demonstrate that MEE precipitation causes NO_x enhancements and ozone destruction through the mesosphere (Andersson et al., 2014; Newnham et al., 2018, 2011; Smith-Johnsen et al., 2018), the magnitude, the interannual-to-decadal variability and the vertical extent of this increase have not been fully characterized. Uncertainty associated with the magnitude and temporal variability of MEE precipitation is due to difficulties in monitoring electron fluxes over the whole energy spectrum (e.g., Mironova et al., 2019, 2015; Rodger et al., 2010). Consequently, a weakness in model studies has been the lack of a robust parametrization of MEE precipitation. Nevertheless, during the last decade, improvements in the analyses of satellite data have allowed a better representation of MEE precipitation. For example, Van De Kamp et al. (2016) developed a new parametrization for MEE precipitation based on geomagnetic indices to provide the climate modelling community with a consistent historical forcing data set from 1850 to 2015, as well as projections to 2299 (Matthes et al., 2017). Hence, for the first time, a consistent data set of solar forcing variables including MEEs, will be taken into account among the factors of natural variability in the 6th Assessment Report by the Intergovernmental Panel on Climate Change (IPCC). Introducing MEE in addition to the auroral electron and SPE fluxes, all of which can potentially destroy mesospheric and stratospheric ozone, could allow current climate models to better capture the effects of EPP.

Current literature on the dynamical impact of ozone perturbations induced by the geomagnetic components of EPP (i.e., auroral electrons and MEE) still lacks consensus. In the southern hemisphere (SH), Tomikawa (2017) extracted EPP-related signals from the Japan Reanalysis data (JRA-55) using regression methods over the period 1979–2010 and found a polar vortex deceleration in the upper stratosphere, but only in July. In atmosphere-only model studies, Semeniuk et al. (2011) and Kvissel et al. (2012) found a winter or spring weakening of the modeled polar vortex caused by EPP, while Rozanov et al., 2005 found an annual-mean strengthening. In a coupled atmosphere-ocean model study focusing on years 2002–2005, Arsenovic et al. (2016) showed a significant weakening of stratospheric winds up to 10 hPa in winter, and a non-significant strengthening in the mesosphere. In the northern hemisphere (NH), Arsenovic et al. (2016) found a significant strengthening of the winter mean stratospheric westerlies, consistent with an earlier model study by Baumgaertner et al. (2011) and with Seppälä et al. (2013), who used re-analysis data covering the years 1957–2008. On the contrary, Semeniuk et al. (2011) showed a jet weakening in the polar region with the jet shifted equatorward and with an opposite mesospheric signal. Meraner and Schmidt (2018) highlighted the importance of month-to-month variability due to both radiative and dynamical processes, with the impact on the stratospheric jet reversal over the course of the winter. The substantial differences

among existing studies in the prescription of the EPP forcing, in intrinsic model dependencies as well as in the period under consideration, may have led to these discrepancies. There is also a lack of support in the observational record due to the relatively short period of continuous stratospheric observations.

The divergent conclusions for the stratospheric impacts indeed lead to different conclusions on whether EPP has a noticeable impact on surface climate. Using reanalysis data and model simulations respectively, Seppälä et al. (2009) and Baumgaertner et al. (2011) concluded that the surface impact of geomagnetic forcing was significant and influenced the North Atlantic Oscillation or Northern Annular Mode. Other studies have shown substantially weaker surface signals (Arsenovic et al., 2016; Meraner and Schmidt, 2018; Rozanov et al., 2012).

The aim of this paper is to improve our understanding of the MEE impact on the decadal time scale climate variability by estimating how, and to what extent, the MEE-induced stratospheric ozone losses might feedback on the dynamics of the middle atmosphere and the troposphere over the 11-year solar cycle. Our focus is on the solar cycle-mean differences, and not on inter-annual variations during the cycle. To this end, we carry out an ensemble of model simulations over a full 11-year solar cycle, with and without MEEs, using a high-top chemistry-climate model called the Whole Atmosphere Community Climate Model (WACCM). To characterize MEEs, we apply the forcing data set provided for Coupled Model Intercomparison Project Phase 6 (CMIP6), since it is likely to be widely used by the climate modelling community. To remove the variability inherent in transient historical simulations, we instead conduct timeslice simulations for pre-industrial conditions. First, the SSTs are climatological, derived from a monthly climatology over the period 1870–1890. Secondly, our simulations are carried out with low emissions of Greenhouse Gases (GHG) and Ozone Depleting Substances (ODS) (e.g., the stratospheric chlorine/bromine levels). By doing so, we remove complexities due to evolving ODS and GHG, which may mask or interfere with fundamental feedback processes. Jackman et al. (2000) pointed out that the chlorine loading actually matters for the long-term impact of strong SPEs. Hence, the low levels of ODS in our simulation might affect our modeled O_3 changes compared to a present-day situation. We also neglect the disruptive effects of large volcanic eruptions and variations due to the Quasi-Biennial Oscillation. We consider both hemispheres and seek to emphasize any interhemispheric differences in assessing the impact of the particle forcing. Using an atmosphere-only model here with prescribed SSTs naturally neglects potential oceanic feedbacks, but this omission is a necessary prerequisite to future coupled atmosphere-ocean modelling efforts of EPP effects.

2. Model description, set-up and experiment design

As part of the Community Earth System Model (CESM) version 1.1, WACCM (version 4) is a fully interactive chemistry and dynamical model (Marsh et al., 2013). Its vertical domain extends from the surface to 5×10^{-6} hPa (or a geometric height of about 140 km) and is divided into 66 layers of variable vertical resolution. We use a horizontal resolution of $1.^\circ$ latitude by $2.^\circ$ longitude. Detailed descriptions of WACCM can be found in previous studies focused on solar effects (e.g., Marsh et al., 2007) and in the WACCM 4 documentation (Neale et al., 2012). In particular, the model includes a gravity wave parametrization of orographic and non-orographic (convective and frontal) sources (Richter et al., 2010). It also includes the neutral middle atmosphere chemistry based on the Model for Ozone and Related Chemical Tracers, version 3 (Kinnison et al., 2007). Above ~65 km, a simple ion chemistry incorporates five positive ions (O^+, O_2^+, N^+, N_2^+, NO^+) as well as electrons. The ion pair production rates by electrons in the auroral regions are calculated by a parametrization based on hemispheric power (HP),

linking empirically HP and the Kp planetary geomagnetic index (Zhang and Paxton, 2008). The production of NO_x and HO_x by EPP and the ensuing ozone destruction by catalytic cycles is further described in Marsh et al. (2007). The MEE precipitation allows for additional NO_x production into the D-region, below 90 km. Since there is no D-region ion chemistry in the standard WACCM, no extra ions are produced, and the production of excited nitrogen is directly parametrized from the energy of the incoming electrons (see Neale et al. (2012) for details).

For consistency, all the solar and geomagnetic forcings in our simulation are specified based upon recommendations for CMIP6 (Matthes et al., 2017). The CMIP6 dataset provides MEE ionization rates derived from a model that uses the observed geomagnetic Ap index as its only input (Van De Kamp et al., 2016). The ionization rates are zonally averaged in geomagnetic latitudes, providing spatial representation of where EPP is occurring under the auroral belts, yet without accounting for dependency on magnetic local times. We choose to solely simulate solar cycle 23 (1996–2008). This choice is based on an examination of the historical cycles from 1855 to 2008, which are included in the CMIP6 dataset. The cycle-mean solar radio flux (f10.7) and ionization rates from MEEs during solar cycle 23 are similar to the corresponding averages of these cycles. For simplicity, we only perform analysis from diagnostics on the full calendar years of the cycle (i.e., 1997–2007). We exclude particle precipitation from SPEs to isolate the MEE signal.

We designed two experiments, one without MEE forcing (control run) and one with the aforementioned MEE forcing (MEE experiment). Each simulation starts at the same date, following a spin-up period of 18 months. To reduce uncertainties due to internal dynamical variability, each experiment consists of an ensemble of 20 11-year simulations. Following the procedure in CESM Large Ensemble Project (Kay et al., 2015), each ensemble is generated by applying small initial temperature perturbations of the order of 10^{-14} K, sufficient to produce independence among the members.

The prescribed SSTs are climatological but seasonally evolving, derived from a monthly climatology of the HadOIBI dataset over the period 1870–1890.

Dynamical diagnostics of wave-mean flow interaction are based on the Eliassen-Palm (EP) flux and the Transformed Eulerian Mean formalism (Andrews et al., 1987). The mean flow forcing is decomposed into a first term which is the EP flux divergence, hereafter referred to as the PW drag (PWD), since it is largely dominated by planetary waves (PWs). A second term is the parametrized gravity wave (GW) drag (GWD), which dominate the wave-mean flow interactions in the mesosphere. The PWD and the associated residual circulation are calculated using daily data, while GWD is pre-calculated in WACCM.

In the following section, we show the monthly climatology of the ensemble mean differences between the MEE experiment and the control run. The monthly climatology is hence based on a set of 220 realisations for each calendar month. Statistical significance testing on these differences is carried out by performing a permutation test: the actual difference between the two experiments is compared to the distribution of randomized differences constructed from the ensemble members of both experiments. The comparison is done for a 95% confidence level.

3. Results

3.1. Forcing by MEE

Fig. 1a and b shows polar maps of the annual mean NO_x (N + NO + NO_2) field (black contours) in the MEE experiment at 90 km. Fig. 1c and d illustrate the corresponding anomalies (defined as MEE experiment minus control experiment). The region of $N(^2D)$ annual mean production rate associated with MEE forcing is indicated with red shadings. As

the MEE forcing is symmetrical in geomagnetic coordinates, there is a longitudinal asymmetry in the production of $N(^2D)$ in geographic latitudes, due to the shifts of the magnetic poles. This asymmetry is reflected in the NO_x anomalies (Fig. 1c and d), but only weakly in the total NO_x field in the MEE experiment, suggesting that mechanisms other than MEE production (e.g., radiation and transport) dominate the overall NO_x distribution. The NO_x anomalies are less than 10% of the background NO_x. We also note that the $N(^2D)$ isopleths are more aligned along geographical latitudes in NH than SH, since the geomagnetic latitudes are more parallel with geographic latitudes in NH. Hence, larger $N(^2D)$ zonal-mean production rates occur at 70^0 N than at 70^0 S. This is confirmed in Fig. 1e and f, showing the longitude-height cross-sections of the annual mean $N(^2D)$ production rates (filled contours) and the NO_x anomalies (line contours), at 70^0 in both hemispheres between 60 and 90 km. We clearly see the distinctive longitudinal asymmetry in the SH giving rise to two separate $N(^2D)$ maxima as compared to the more uniformly distributed high $N(^2D)$ sector in the NH, reflecting to which extent the forcing regions in Fig. 1c and d map onto geographical latitudes, near the 70th parallel. The longitudinal asymmetries in $N(^2D)$ production are mirrored in the NO_x anomalies between 80 and 90 km, where high NO_x anomaly coincides with high $N(^2D)$ production. Below those levels however, as the $N(^2D)$ production substantially weakens, the longitudinal anomalies in NO_x do not merely mirror the zonal asymmetries of the MEE forcing, and other factors control the NO_x distribution.

3.2. Impact on O_3 and related chemistry

Fig. 2 shows the monthly-mean O_3 volume mixing ratio anomalies (in ppmv as filled contours) along with O_3 from the control experiment (line contours, in ppmv) in the stratosphere and MLT (20–100 km), averaged over the 70°–90° latitude band in both hemispheres. The statistically significant region (at the 95% confidence level) is indicated by black dots. In the secondary O_3 layer near 90–100 km, a distinct negative anomaly is visible in NH (up to 0.15 ppmv or 3.5%). In the mesosphere, we note a significant wintertime O_3 deficit in both hemispheres in the tertiary O_3 layer between 65 and 80 km. The O_3 deficit is slightly larger in NH (up to 0.25 ppmv or 15–20%) than in SH (up 0.20 ppmv or 10–15%). In the main stratospheric O_3 layer, which maximizes between 30 and 45 km, the O_3 deficit is weaker than in the tertiary O_3 layer, but nevertheless significant in both hemispheres. This deficit is more pronounced in the SH (up to 0.15 ppmv or 2% while 0.1 ppmv or 1% in NH). The descent of the O_3 negative anomaly throughout the winter and spring is also clearer in SH, where the polar stratosphere is less impacted by dynamical variability. The magnitudes of these O_3 decadal-mean deficits are consistent with those found in a coupled ocean-atmosphere CMIP-5 historical simulation over the years 1950–2010 by Andersson et al. (2018), who used the same WACCM version and CMIP6 forcing as here.

To investigate processes governing the mid-winter stratospheric O_3 deficit, we focus on NO_x anomalies since the NO_x catalytic cycle is the dominant ozone-depleting cycle in the upper stratosphere. The NO_x lifetime is sufficiently long in the polar night so it can be transported from its production region downward into the upper and mid-stratosphere. With the additional $N(^2D)$ production in the MEE run (see Fig. 1), we expect an enhancement in NO_x volume mixing ratios. The corresponding cross-section of the anomalous NO_x mixing ratios (in ppbv) is shown in Fig. 3 in the 20–60 km range. Fig. A1 is the equivalent figure for odd nitrogen (NO_y: N + NO + $NO_2+NO_3+2*N_2O_5+HNO_3+HO_2NO_2+ORGNOY + NH_4NO_3$). Starting from above the stratopause region, a tongue of positive NO_x (or NO_y) anomalies indicative a higher abundance in the MEE run descends
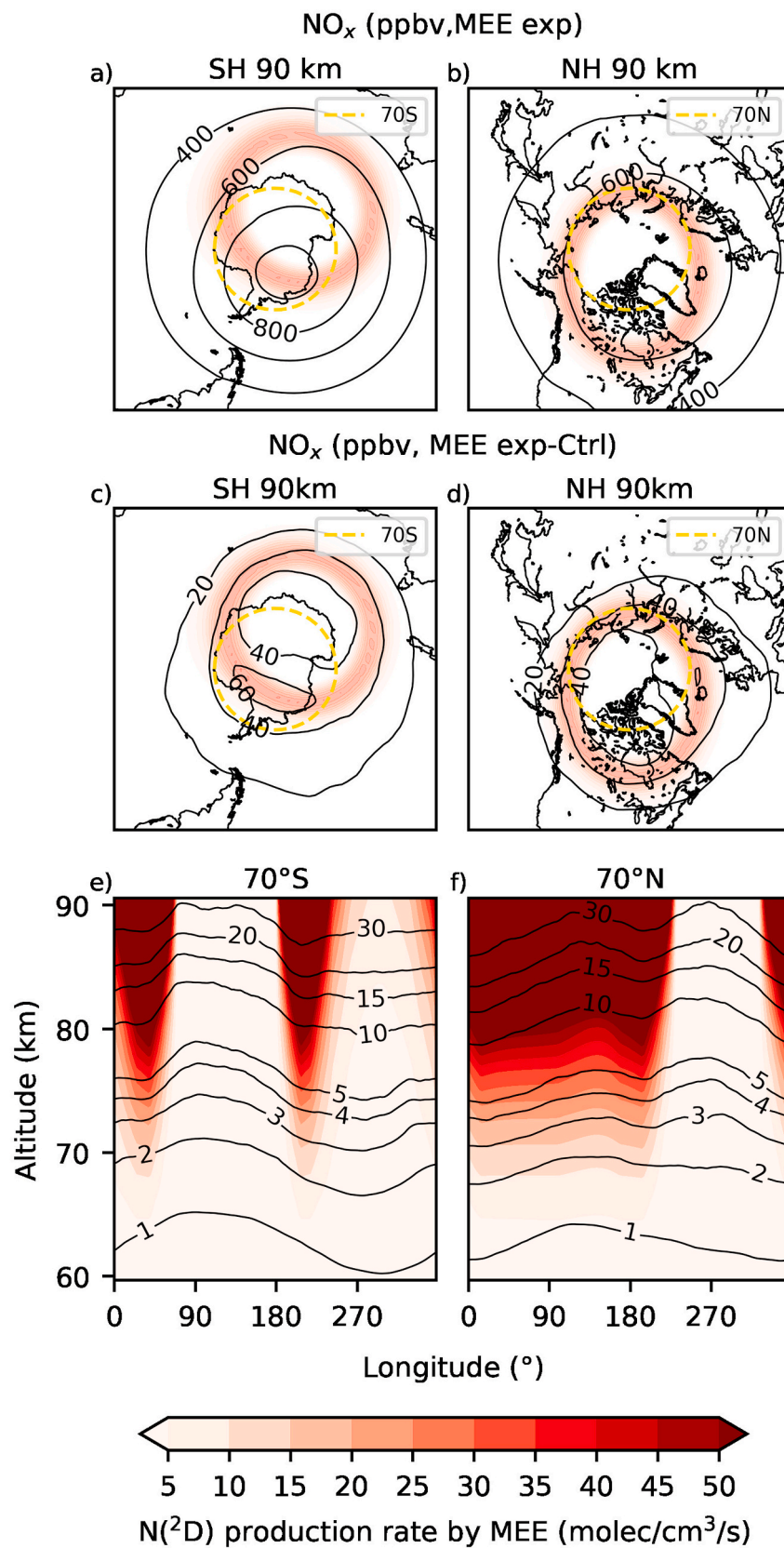
NO_x (ppbv, MEE exp)

Fig. 1. (a,b) Annual mean of NO_x mixing ratios (ppbv, black contours) in the MEE experiment in both hemispheres at 90 km. $N(^2D)$ production region is indicated by red shadings. The yellow dashed circle represents the 70^0 N/S latitude. (c,d) As (a,b), but the NO_x field is the anomaly between the MEE experiment and the control run. (e,f) Annual mean of $N(^2D)$ production rates by MEE (molec/cm^3/s, red filled contours) and NO_x anomalies (ppbv, black contours), at 70° in both hemispheres.
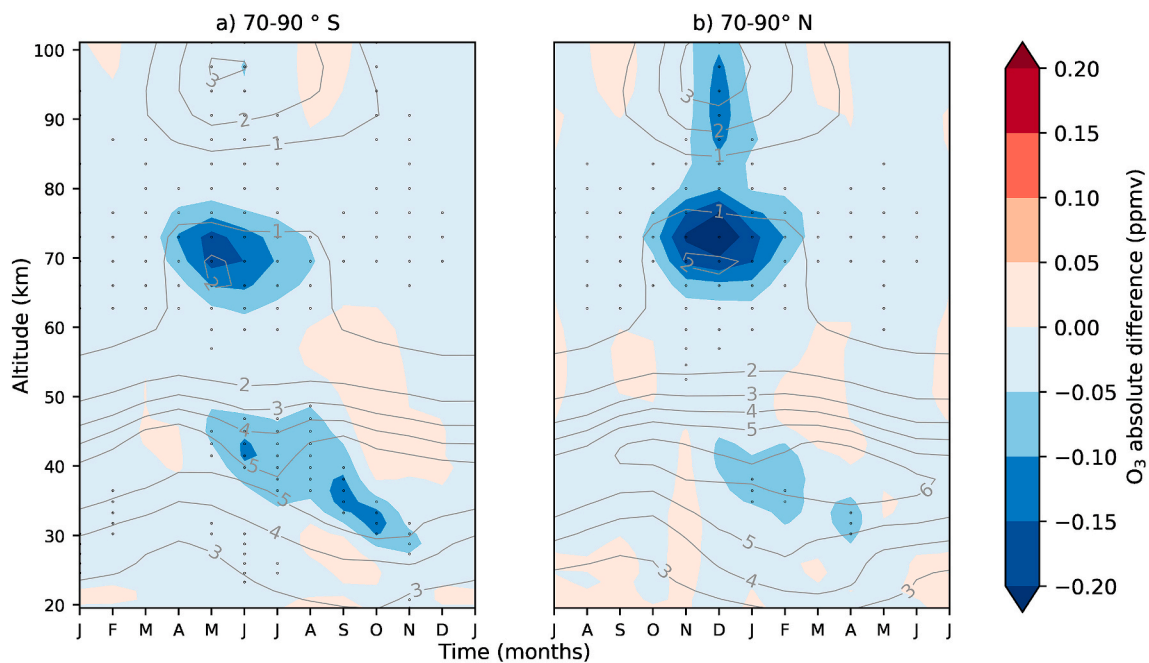
Fig. 2. Climatological annual cycle of the monthly zonal-mean O_3 anomalies (ppmv, in filled contours) and absolute O_3 from the control run (ppmv, gray contours), averaged over latitudes between (a) 70°-90° S and b) 70°-90° N. Black dots represent locations of statistically significant anomalies.

Fig. 3. Climatological annual cycle of the monthly zonal-mean NO_x anomalies (ppbv, in filled contours) and absolute NO_x from the control run (ppbv, gray contours), averaged over latitudes between (a) 70°-90° S and b) 70°-90° N. Black dots represent locations of statistically significant anomalies.
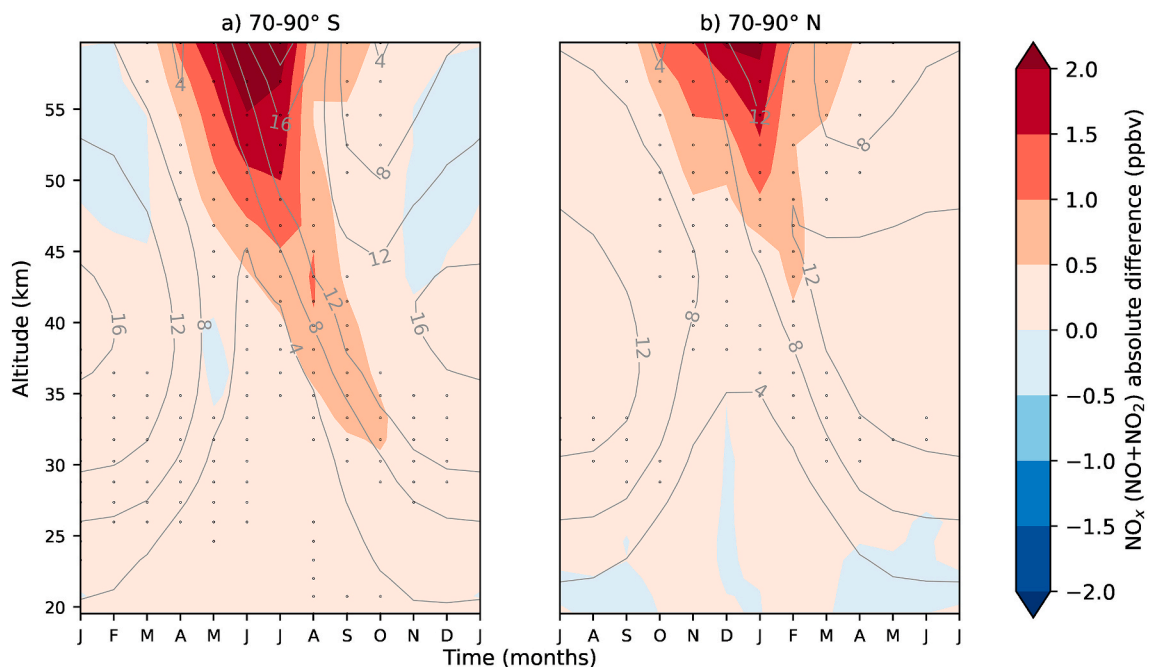
through winter and spring, coinciding with the negative O_3 anomaly in Fig. 2. This descent is stronger and to a greater depth in SH, where it remains significant down to 30 km, consistent with previous model studies (e.g., Andersson et al., 2018; Kvissel et al., 2012) and satellite observations (e.g., Sinnhuber et al., 2018; Funke et al., 2014). The magnitude of the decadal-mean NO_x (or NO_y) anomalies obtained from comparing simulations with and without MEE in Fig. 3 cannot be directly compared with observations, but their magnitudes are broadly consistent with the aforementioned studies.

Fig. 4 shows maps of NO_x and O_3 anomalies (as filled contours, in ppbv and ppmv, respectively) and the corresponding abundances in the control run (gray line contours) for July (SH) and for December (NH). The fields are vertical averages between 40 and 45 km in SH and 38 and 42 km in NH. The rationale behind these altitude selections is that the most prominent O_3 deficits occur in these altitudes. Also shown are the geopotential heights from the control run delineating the polar vortex (black line contours on the NOx plot), and the Short Wave Heating Rates (SWHR) anomalies (in K day^{-1}, white line contours, on the O_3 plot).
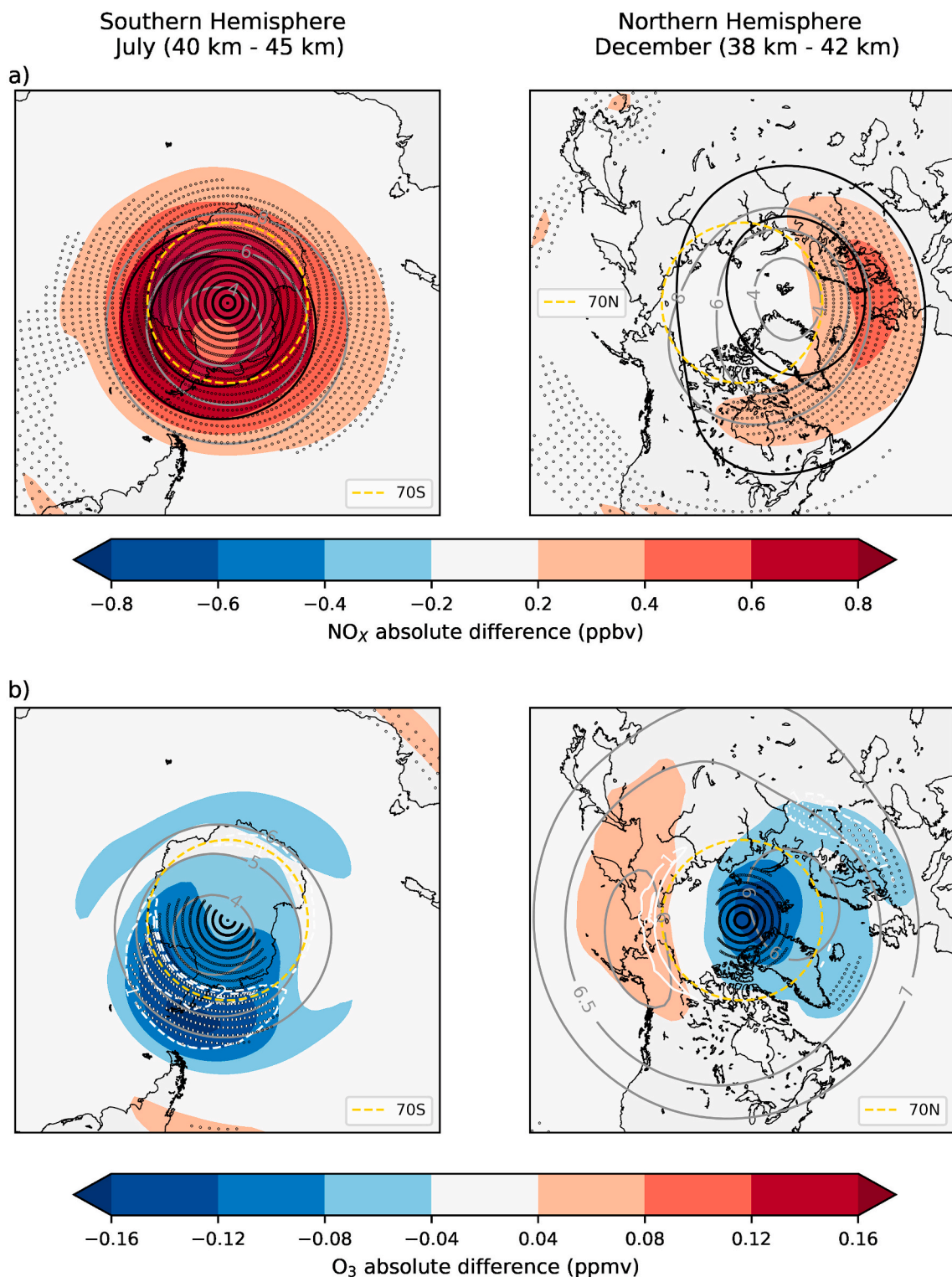
Fig. 4. Climatological monthly mean of (a) NO_x (ppbv) and (b) O_3 (ppmv) anomalies (filled contours) and the corresponding absolute field from the control run (gray contours) in SH in July and in NH in December. The fields are pressure-weighted vertical averages between 40 km and 45 km in SH and 38 km and 42 km in NH. The yellow dashed circle represents the 70^0 N/S latitude. Black dots represent locations of statistically significant anomalies. Black contours in (a) localize the polar vortices as geopotential heights. Short Wave Heating Rates relative anomalies (-2, -1, and 1%, white contours) are shown in (b) with indication of statistical significance (white dots).
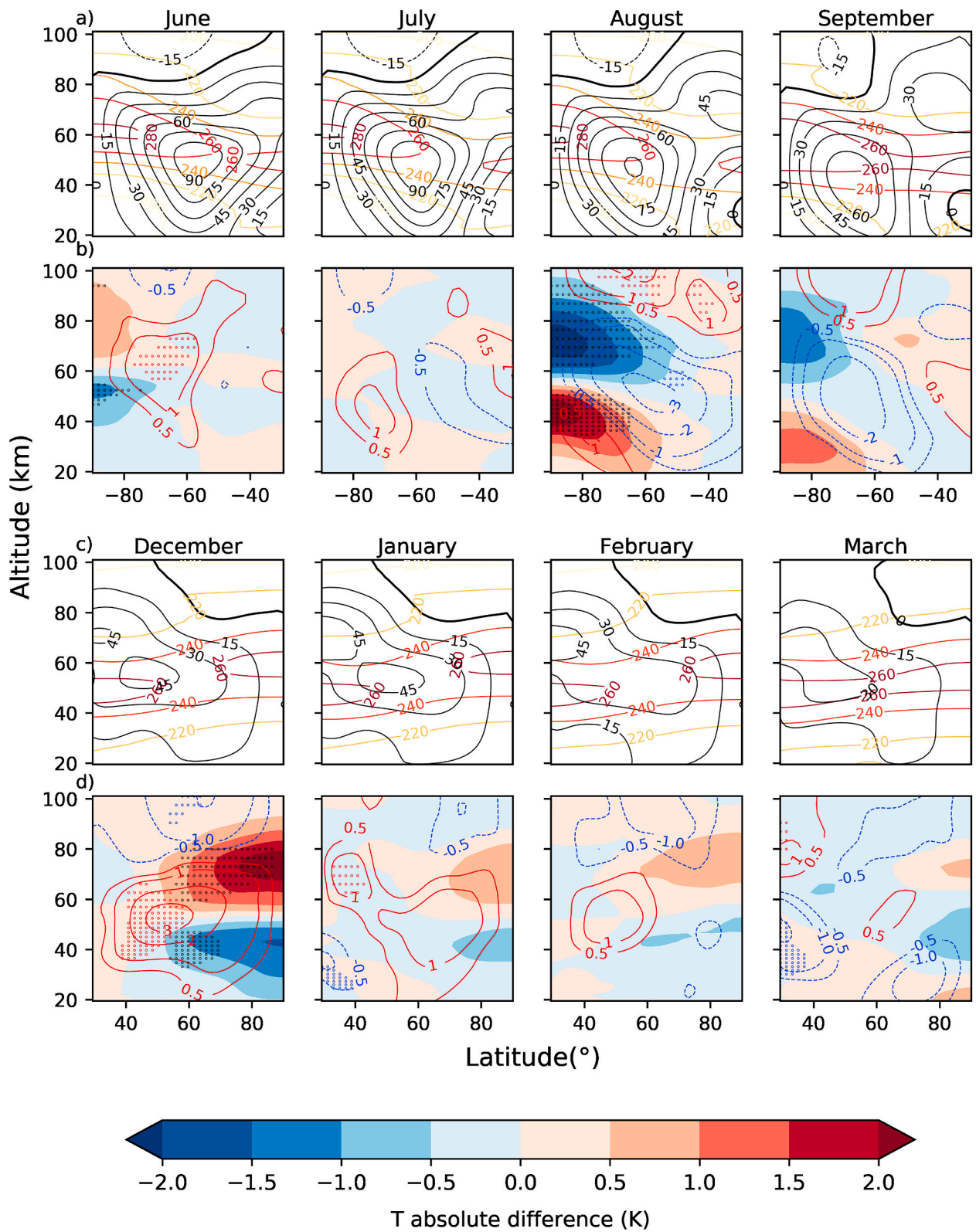
Fig. 5. Climatological monthly-mean zonal-mean temperature field from the control run (K, yellow-red contours) along with the absolute zonal wind field from the control run (ms^{-1}, black contours) in (a) June–September in SH and c) December–March in NH. The corresponding temperature anomalies (K, filled contours) along with the wind anomalies (m/s, red and blue contours) are shown in (b) June–September in SH and (d) December–March in NH. The wind anomalies show magnitudes above± 0.5 ms^{-1}. Black (colored) dots represent locations of statistically significant temperature (zonal wind) anomalies.

In both hemispheres, the regions with significant O_3 deficit extend to the highest latitudes and even to the poles, especially in NH. We surmise that these polar deficits, and to some extent the O_3 anomalies outside the polar vortices, result from transport processes, an issue that we will address below. Further examination of Fig. 4b reveals the presence of weak but nevertheless significant negative O_3 anomalies in sub-polar regions is, in the first place, likely a result of O_3 chemical destruction (i.e., true loss) by the NO_x catalytic cycle, when air masses are advected into sunlit regions. This effect is most striking in NH, where the climatological polar vortex is more zonally asymmetric than in SH, with its center shifted towards Eurasia. In SH, these regions with significant sub-polar ozone losses are mostly toward South America, where the sub-polar NO_x anomalies are also large. Furthermore, the SWHR negative anomalies in these subpolar regions (white contours in Fig. 4b) mostly coincide with the significant O_3 losses. This is expected since O_3 is a main absorber of solar radiation at these altitudes. The O_3 anomalies displayed in Figs. 2 and 4 are important to explain the radiative-dynamical impacts from the MEE forcings, as will be described in the following sections.

3.3. Impact on temperature and zonal wind

We now turn our attention to the MEE impact on the temperature and the circulation. Fig. 5a,c shows the winter-to-spring evolution of the zonal-mean temperatures and zonal winds from the control run from 20 km to 100 km (red/orange contours and black contours, respectively) poleward of 30^0 for SH and NH. Corresponding temperature and zonal wind anomalies are shown in Fig. 5b,d (filled contours and red/blue line contours, respectively). Statistically significant anomalies are indicated as black dots for temperature and as colored dots for zonal wind.

During the first winter month (June in SH and December in NH), Fig. 5b,d reveal vertical dipoles of temperature anomalies characterized by a mesospheric warming (as much as 2.5 K in NH and 0.5 K in SH) and a stratospheric cooling (as much as 1.5 K in NH and 1.0 K in SH). The dipoles are located poleward of 75^0 in SH and of 55^0 in NH. Except for the mesospheric increase in SH, the vertical dipoles in each hemisphere are significant. The stratospheric temperature anomalies indicate that the negative meridional temperature gradient between the mid-latitudes and the polar region is more pronounced in the MEE run compared to the control run (i.e., the cold pole is even colder). By thermal wind balance, this gradient corresponds to a positive zonal-mean zonal wind vertical shear and, hence, an intensification of the westerlies. Similarly, in the mesosphere, the positive meridional temperature gradient between the mid-latitudes and the pole is enhanced (i.e., the warm pole is even warmer), corresponding to a negative zonal wind vertical shear. In NH, the December wind anomalies reach over 3.0 m s^{-1} while in SH, the June wind anomalies are over 1.5 m s^{-1}.

In NH, the anomalous temperature vertical dipole and the corresponding wind intensification seen in December persist weakly into January and February but are not significant then. However, the SH temperature dipole anomaly switches sign and becomes larger (up to

Table 1
Climatological monthly-mean zonal-mean eddy component (deviations from zonal mean) of O_3 (ppmv), Short Wave Heating Rates (K day^{-1}) and Temperature (K) for the control run, MEE experiment and the relative difference (MEE-Ctrl, in %). All the fields are averaged between $50°$ and $70°$ latitude at 42 km in July in SH and 40 km in December in NH.

	July (SH)			December (NH)		
	Ctrl	MEE	Mee-Ctrl (%)	Ctrl	MEE	MEE-Ctrl (%)
Ozone (ppbv)	0.30	0.32	+7	0.19	0.16	−16
Short Wave Heating Rates (K/day)	0.039	0.040	+3	0.042	0.039	−7
Temperature (K)	9.0	9.5	+6	8.2	7.7	−6

2.5 K) in August. This reversal and enhancement of temperature anomalies in August are associated with zonal wind anomalies (reaching over 3.0 m s^{-1}) opposite to those during the first winter month, but significant mostly in the polar mesosphere. These temperature and zonal wind anomalies subside by September. In comparison to previous studies, which often focused on winter means, our results indicate important month-to-month variations likely caused by different processes (further discussed below).

To further elucidate the origin of the decadal-mean zonal-mean zonal winds anomalies, we examined the histograms (see Fig. A2) of daily high-latitude winds in both experiments spanning an ensemble of 220 winters (of 20 11-year members), focusing on the winter jet intensification (December–February in NH and June–July in SH), and the late winter-spring weakening (August–September in SH). The months, altitude and latitude were determined from Fig. 5. During the two jet intensification periods, the mean jet increase in the MEE experiment can be attributed to higher occurrences of high winds at, and higher than, the maximum of the distribution and decreased occurrences of weak winds. The opposite holds during the jet weakening period (August–September in SH), although this is not reflected at the maximum of the distribution in this case. We further verified that the monthly-mean wind differences in the NH high latitudes in Fig. 5 are not caused by different occurrences of sudden stratospheric warmings (SSWs) in the two ensemble experiments. In particular, we did not find any differences in the sign of the anomalies when excluding SSWs, and noted only small changes in their magnitudes in all but for one month (See Table A1).

3.4. Impact on wave forcing and residual mean meridional circulation

The winter-to-spring evolution of the anomalous residual mean meridional circulation and total wave forcing (from PWD and GWD) is displayed in Fig. 6a for SH in June–September 6b for NH in December–March. Vectors and line contours illustrate the circulation and wave forcing, respectively. The zonal-mean temperature anomalies are repeated for ease of interpretation (filled contours, identical to Fig. 5b and d). We also show the respective contributions of the PWD and GWD to the total wave forcing in Fig. A3.

In NH, the anomalous positive total wave forcing in December (indicative of reduced westward forcing) between 45 km and 60 km coincides with the positive zonal wind anomaly seen in Fig. 5d. This positive forcing largely arises from the PWD (see Fig. A3). A westward forcing is found in the overlying layer between 65 km and 100 km. This opposite westward forcing can be explained by the more effective filtering of eastward GWs by the anomalously strong upper-stratospheric westerlies. This filtering allows for an increased westward GWD in the MLT. Depending on the location of the zero-wind line, which varies with latitude and height (Fig. 5c), this westward anomalous GWD contributes to a decrease of the background westerlies (e.g. below 80 km in the polar regions) and increase of the background easterlies aloft. A similar mechanism (increased westerlies and opposite westward GWD aloft) was also found by Cullens et al. (2016) in their examination of the solar cycle modulation in WACCM. The early winter positive wave forcing anomaly is located slightly higher in the mesosphere in SH (Fig. 6a), and above we find the same GW filtering mechanism as in NH.

Along with the aforementioned reduction in westward wave forcing in the upper stratosphere-lower mesosphere during the first winter month, the stratospheric part of the residual circulation is weakened, with anomalous polar upwelling accompanied by cooling. This anomalous upwelling is weaker in the SH, in line with the weaker and less extensive wave drag anomalies. On the other hand, in response to the anomalous westward GWD, the mesospheric meridional circulation increases substantially in both hemispheres with poleward motion in midlatitudes and downwelling and adiabatic warming at high latitudes. The dipole structure in temperature anomalies (see in Fig. 5 or 6) appear to be linked to those anomalous mean meridional circulations driven by
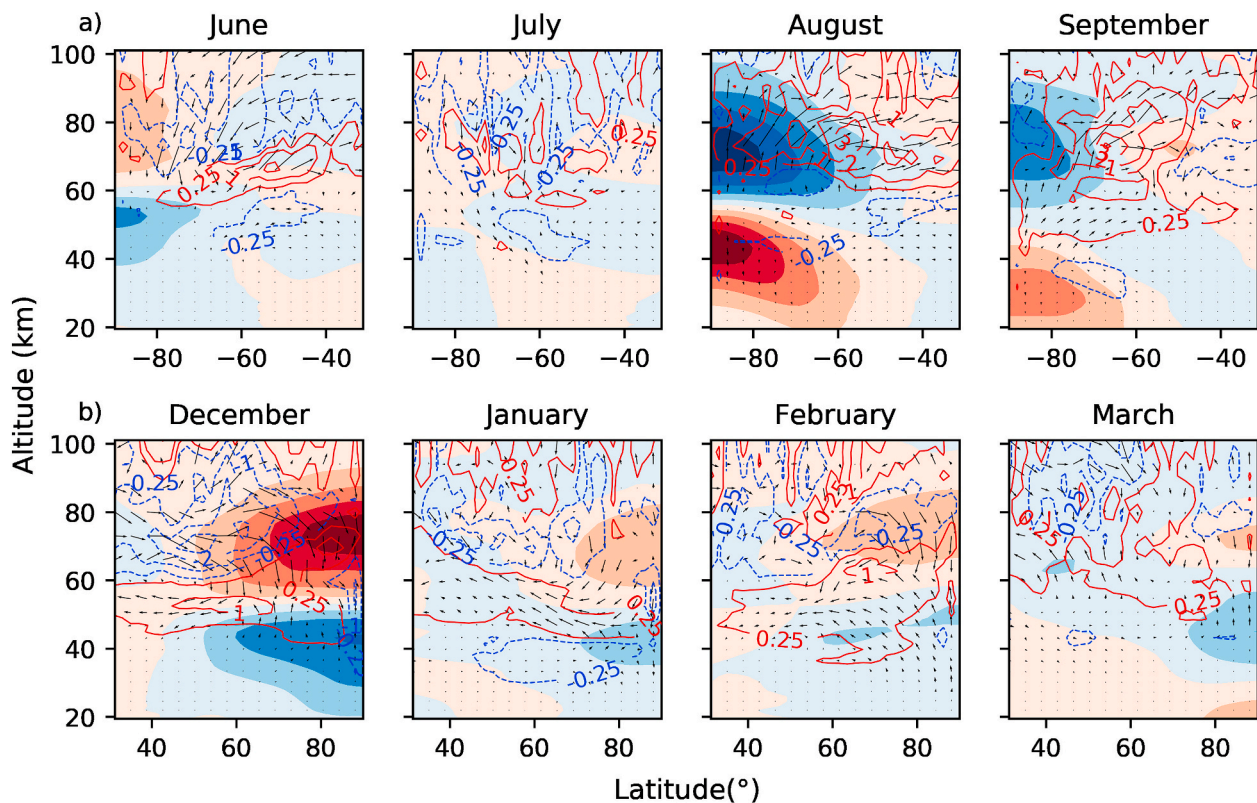
Fig. 6. Climatological monthly-mean total wave forcing (PWD + GWD) anomalies (ms^{-1}day^{-1}, red and blue line contours) along with the anomalies of the residual mean meridional circulation (vectors) and zonal-mean temperature anomalies (K, filled contours, see colorbar in Fig. 6) in (a) June–September in SH and (b) December–March in NH. The total wave forcing contours show magnitudes above±0.25 ms^{-1}day^{-1}. The vectors are equally scaled across all plots.

PWD and GWD. In the polar upper stratosphere however, the dynamically-driven cooling is counteracted by radiative warming, since we expect reduction in longwave radiative cooling (i.e., warming) associated with negative O$_3$ anomalies seen in Figs. 2 and 4. From the larger stratospheric O$_3$ deficit in SH (see Fig. 2a), we expect the ozone radiative effect to be stronger in SH. The observed cooling rates in mid-winter (albeit available in NH) are relatively strong (0.5–1.0 K day^{-1}) for this altitude region (Brasseur and Solomon, 2005). Hence, acting in concert with the weaker wave forcing, this stronger radiative effect might explain the weaker temperature anomalies in SH.

In the following months (i.e., July–September in SH and January–March in NH), the zonal wind and temperature anomalies behave differently between the two hemispheres (see Fig. 5b and d). In NH, the early winter signal merely declines, predominantly after January. In addition to the subsiding wave forcing anomalies, the polar cap O$_3$ deficit resulting in upper stratosphere radiative warming might also contribute to the weaker signal. In SH, following the weakening in July, the strong decrease of the jet in August (seen in Fig. 5b) is not accompanied by a correspondingly strong PWD anomaly. However, the residual mean meridional circulation in the mesosphere is clearly reduced, resulting in anomalous adiabatic cooling in the polar mesosphere in August. The aforementioned reduced longwave cooling attributable to the polar O$_3$ deficit (see Fig. 2), beside the weak PWD anomalies, is also a plausible explanation for the temperature and zonal wind anomalies in the stratosphere. This radiatively induced anomalous warming reduces the meridional temperature gradient, which in turn weakens the westerly flow. Consistent with the GW filtering due to weakened westerlies,

an increased opposite (eastward) GWD appears aloft in the upper mesosphere (see Fig. A3b), consistent with the reduced poleward motion and reduced mesospheric adiabatic heating. Simultaneously in the stratosphere, poleward motion and polar downwelling increase, adding to the radiatively-induced temperature increase. This process may stop by September with the return of insolation at high latitudes, when UV absorption comes into play. Less O$_3$, then, would be associated with reduced heating, and this cooling anomaly would counteract the stratospheric heating.

3.5. Role of zonal asymmetries in ozone

From the zonal-mean perspective, we see that the anomalous PWD (as seen in Fig. 6) triggers the dynamical changes observed in Fig. 5, though most predominantly in early winter in NH. Previous studies (e.g., Kvissel et al., 2012; McCormack et al., 2011; Peters et al., 2015; Waugh et al., 2009) pointed out that taking into account ozone zonal asymmetries is important to accurately represent the vertical propagation of wintertime PWs into the stratosphere in both hemispheres, as they are associated likewise with zonal asymmetries in short-wave heating and in temperatures at mid- and subpolar latitudes.

As shown in Fig. 4, O$_3$ is asymmetrically disturbed at mid- and subpolar latitudes, with similar zonal asymmetries in SWHR. In NH, the negative O$_3$ anomaly is found over Europe, a longitude sector associated with an O$_3$ maximum in the control run. In other words, the zonal asymmetry is reduced in December in the MEE run. On the other hand, in SH, we find an increase in the zonal asymmetry in July as the crescent-
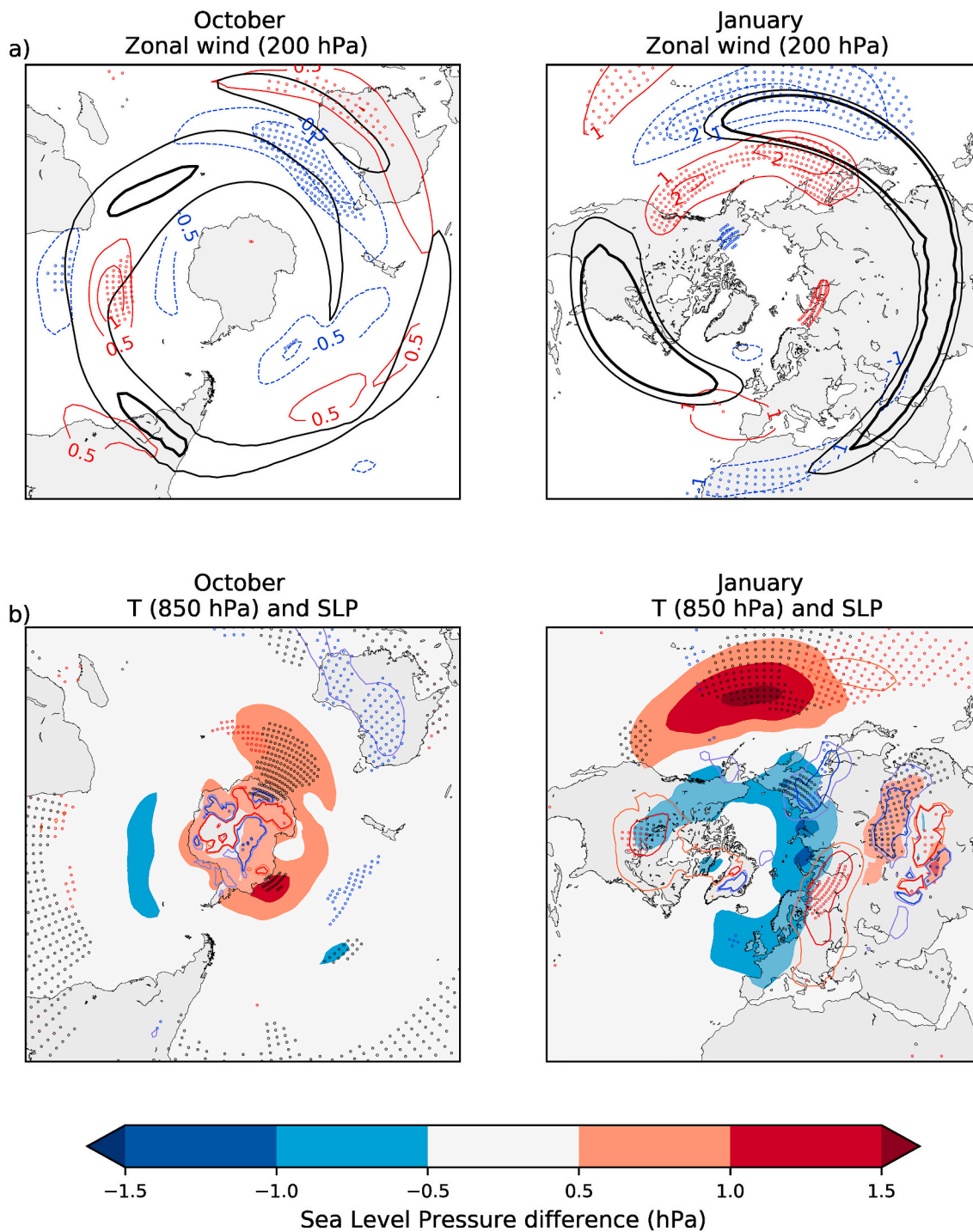
Fig. 7. Climatological monthly mean of zonal wind anomalies (ms^{-1}, blue and red line contours) at 200 hPa from October (SH) and January (NH) in (a). Zonal wind from the control run (black contours) localize the climatological jets. Climatological monthly mean of temperature anomalies (−0.5,-0.25,0.25,0.5 K, blue and red line contours) at 850 hPa and surface pressure anomalies (hPa, filled contours) are shown for the same months in (b). Colored dots in (a-) represent locations of statistically significant zonal wind anomalies. Colored (black) dots in (b) indicate statistically significant temperature (surface pressure) anomalies.

shaped negative O_3 anomaly is found in regions with low O_3 abundances.

The increase or decrease of zonal asymmetries in O_3 and in associated heating rates are consistent with the main dynamical signals found in Figs. 5 and 6, i.e., reduced PWD and strengthening of the NH polar vortex in December–January and the opposite effect in August–September in SH. To quantify this zonal asymmetry in O_3 and relate it to PWD anomalies at subpolar latitudes (displayed in Fig. A3), Table 1 shows the eddy component (deviation from the zonal mean) of the monthly-mean O_3, SWHR and temperature in July (SH) and December (NH) for the control and MEE runs and their anomalies. The eddy component is averaged over 50°–70° latitude band, at 42 km in SH and 40 km in NH. In July, the amplitudes in the MEE run surpass those in the control runs, consistent with a weakly increased SH PWD activity in July–August. In December, they are weaker in the MEE run, consistent with a weaker stratospheric NH PWD in December–January.

We note from Fig. 5 that the O_3 maps indicate not only subpolar O_3 loss but also a polar deficit which we attribute to the anomalous mean meridional circulation. In other words, these maps also reflect the dynamical feedback triggered by these eddy disturbances. For example, in NH, a reduced poleward transport limits advection of high O_3 from mid-latitudes into the polar region. In a similar fashion, the eddy component anomalies in Table 1 will also reflect the effects of reduced PWs, limiting our ability to infer causality.

In summary, we suggest that, in NH early winter, a reduction in O_3 zonal asymmetries at subpolar latitudes, induced by higher NO_x abundance through production and descent in the MEE run, lead to weaker PWs and a reduced westward PWD. An opposite, but weaker, increase in O_3 zonal asymmetries might contribute to the increased PWD in SH late winter.

3.6. Tropospheric impacts

In the preceding sub-sections, we looked at the MEE decadal impact on the middle atmosphere chemistry and dynamics. With significant seasonally-dependent dynamical changes in the stratosphere occurring in both hemispheres, a pertinent question is whether MEE-related anomalies appear in the troposphere and potentially influence the surface climate. In Fig. 7a, we show the hemispheric zonal wind upper-tropospheric anomalies (red and blue contours) at 200 hPa in October (SH) and January (NH).The climatological zonal wind indicative of the jet stream position is represented by the thick black contours. In Fig. 7b, we show the corresponding sea level pressure (SLP, filled contours) and temperature (red and blue contours) anomalies. Since the surface temperature was not available in our model output, we show the temperature at 850 hPa. Consequently, the temperature response has to be interpreted with caution, especially over large regions associated with high topography (e.g., over Antarctica, Greenland or the Himalayas). The rationale behind the choice of months is that these tropospheric signatures would be lagged with respect to the main stratospheric wind anomalies found in their winter maximum (August in SH, December in NH).

In SH, we note that the anomalous decrease of the stratospheric westerlies in August–September (see Fig. 5) manifests at 200 hPa in October. However, the relevant wind anomalies (around 60^0 S) are mostly not significant and generally weak, reaching only $-1.0 \, \text{m s}^{-1}$. We also note consistent and significant SLP anomalies over the polar cap (around 0.5–1.0 hPa), which would correspond to a negative anomaly of the southern annular mode.

The dynamical impacts in the NH troposphere are stronger and more complex than in SH. In January, we find a poleward shift of the jet stream (at 200 hPa) over the Pacific Ocean, with zonal wind enhancement of $2.0 \, \text{m s}^{-1}$ on its poleward flank (between 40^0 and 50^0 N) and weakening of $-2.0 \, \text{m s}^{-1}$ on its equatorward flank. Over the Atlantic Ocean, there is a weaker and mostly not significant opposite anomaly limited to the jet exit region, corresponding to an equatorward shift of

the jet stream.

Consistent with the wind anomalies we find several regions with significant temperature anomalies. Areas of cooling (up to -0.5 K) are found on the northern side of the Pacific jet increase, but it is only significant over the Far East, and of warming on its southern side. As expected from increased westerlies bringing warmer oceanic air, there is a temperature increase (up to 0.5 K) over North America downstream of the North Pacific jet, and over Northwest Russia, downstream of the North Atlantic jet, and a weak cooling over the North Atlantic. The corresponding polar SLP anomalies are less zonally symmetric and encompass a lesser portion of the polar cap compared to the SH case. Nevertheless, the anomalous SLP pattern exhibits positive anomalies at mid-high latitudes and projects onto the positive northern annular mode or Arctic Oscillation (AO), which we also have confirmed by a calculation of an AO proxy (not shown). However, we note that the negative pressure anomalies over the North Atlantic associated to the equatorward shift of the 200-hPa jet stream deviate from the canonical positive AO pattern, but these are only weakly significant. The negative SLP anomalies are only significant over the Far East, a region where the strongest and most significant upper-level wind changes appear aloft. Similarly, the mid-latitude positive SLP anomalies expected in an AO positive phase, are not found at all longitudes, but are rather limited to Central Asia and the North Pacific.

4. Summary, discussion and conclusions

In this study, we used the high-top chemistry-climate model with interactive chemistry and dynamics (WACCM) to investigate the impacts of MEEs on the middle atmosphere and the troposphere. We attempted to isolate the MEE effect by excluding other known forcings such as SPEs, large volcanic eruption, SST, and the QBO. The MEE forcing was prescribed by using the time-varying solar and geomagnetic forcing as recommended by CMIP6 (Matthes et al., 2017). We applied an ensemble approach, running twenty pairs of control and perturbed simulations over a period corresponding to solar cycle 23. We focused on analyzing the decadal climate impacts from MEEs by examining the monthly climatology over this period. We analyzed the impact of enhanced NO_x production on ozone, and the interactions between the stratospheric ozone change and the atmospheric dynamics. While previous studies, like Meraner and Schmidt (2018), mostly focused on radiative effects of zonal-mean ozone perturbations, we presented here another pathway involving ozone zonal asymmetries and their impact on PWs.

We focused on stratospheric O_3. The magnitudes of our simulated anomalies in stratospheric O_3 are comparable to those shown in Andersson et al. (2018) and Arsenovic et al. (2016). Our results indicate a strong month-to-month variability in the dynamical response to MEE throughout the winter period. In NH, we found a significant strengthening of the polar vortex in December, decaying rapidly in the following months. The polar vortex strengthening is likely attributable to PW activity reduction due to decreased zonal asymmetries in O_3 heating, initiated by MEE-induced NO_x advected into sunlit regions. The filtering effect of the jet strengthening allows an opposite (westward) GWD in the mesosphere, which acts in conjunction with the PWD to create an anomalous temperature vertical dipole pattern of stratospheric cooling and mesospheric warming over the pole. We note that the size of the NH winter-mean wind enhancement in Arsenovic et al. (2016) and Seppälä et al. (2013) are doubled relative to ours. We identified the similar (albeit weaker) response in the SH in June.

The associated weakening of the residual mean meridional circulation induced by those dynamical feedbacks results in the polar cap ozone deficit in winter. This polar cap ozone deficit is strongest in the SH, leading to greater anomalous radiative warming in the polar region than in NH, and thereby opposing the strengthening of the polar vortex. We suggested that both reduced longwave cooling (i.e., anomalous warming) and a weakly enhanced anomalous PWD forced by the increased zonal asymmetries in ozone heating are both plausible explanations for

the weakened polar vortex in August. The weakened polar vortex is followed by a positive feedback loop allowing for additional weakening in the following sequence: (i) a weakening of the zonal winds trigger an increased eastward GWD and a mesospheric cooling, (ii) the stratospheric residual circulation increases, which enhances downwelling and adiabatic heating in the polar stratosphere, and (iii) the warming (cooling) of the stratosphere (mesosphere) increase the reduction of the meridional temperature gradient which reinforce the initial jet decrease. The predominance of the early winter MEE signal in both hemispheres and the high degree of month-to-month variability in the SH winter have not been highlighted by other studies. We note that Kvissel et al. (2012) similarly found a weakened SH polar vortex in the transition from late winter to spring.

In both hemispheres, the main polar vortex signal seems to migrate downwards into the troposphere and to the surface. In NH, our results indicate a weak surface warming over Northwest Russia and North America and a corresponding cooling over the Far East, along with a poleward shift of the Pacific jet and a less prominent equatorward shift of the North Atlantic jet in its exit region. Along with the accompanying anomalously low pressure over most parts of Arctic, these NH changes project onto the positive phase of the northern annular mode or Arctic Oscillation. In SH, the SLP anomalies in spring resemble the negative phase of the southern annular mode. These overall patterns in both hemispheres are consistent with Seppälä et al. (2009), Baumgaertner et al. (2011), Rozanov et al. (2012) and Arsenovic et al. (2016). and the surface temperature changes over Europe in Rozanov et al. (2012) are comparable to ours. Seppällä et al. (2009), Baumgaertner et al. (2011) and Arsenovic et al. (2016) reported surface signals considerably larger than ours. However, we note these studies differ from ours in that we consider the average decadal MEE effect while they focused on responses to EPP maximum years. While our results reveal very robust decadal climate impacts from MEE, stronger signals are possible during specific years due to the highly variable nature of MEE forcing.

We recognize that we just examined a decadal signal resulting from a weak CMIP6-prescribed forcing. The CMIP6 forcing was validated with observations from POES satellites over the years 2002–2012 (Van De Kamp et al., 2016) but one noteworthy limitation is that the inaccuracy substantially increases for low electron flux levels. Recent studies (Tyssøy et al., 2019; Mironova et al., 2019) underlined the possible underestimation of MEEs in this CMIP6 data set. In particular, Mironova et al. (2019) compared EPP ionization rates retrieved from a balloon experiment with the CMIP6 data set and highlighted the weak ionization rates in the latter. Also, electrons of energy higher than 1 MeV are neglected in this data set, so little MEE flux occurs below 60 km. The validity of the particle fluxes derived from satellite observations in this energy range are still subjected to a large uncertainty, and it is not clear yet if including highly-energetic electrons could potentially induce greater ozone destruction in the middle atmosphere (e.g. Mironova et al., 2019). Consequently, this study provides a lower limit of the MEE impact. Regardless, whether a stronger forcing (amidst the large internal variability and natural external variability driven by other factors) is sufficient to increase the MEE effects on middle atmosphere and surface climate remains an open question.

Finally, we limited our main analysis to stratospheric O_3 and its radiative-dynamical impacts. The role of MEE-induced O_3 anomalies in the tertiary O_3 layer ought to be investigated in future work. There is also a general need to study sub-monthly processes to better understand the causes and effects.

Declaration of Competing Interest

The authors declare that they have no known competing financial interests or personal relationships that could have appeared to influence the work reported in this paper.

Acknowledgements

Appendix

Table A.1

The numbers of SSWs in the control run and the MEE experiment based on the criteria that a minimum of 5 consecutive days with negative winds (<0 m/s) is counted at 50 km at 60° latitude in December–March in NH and June–September in SH. The anomalies (MEE-Ctrl) at the same height and latitude are shown with and without SSWs.

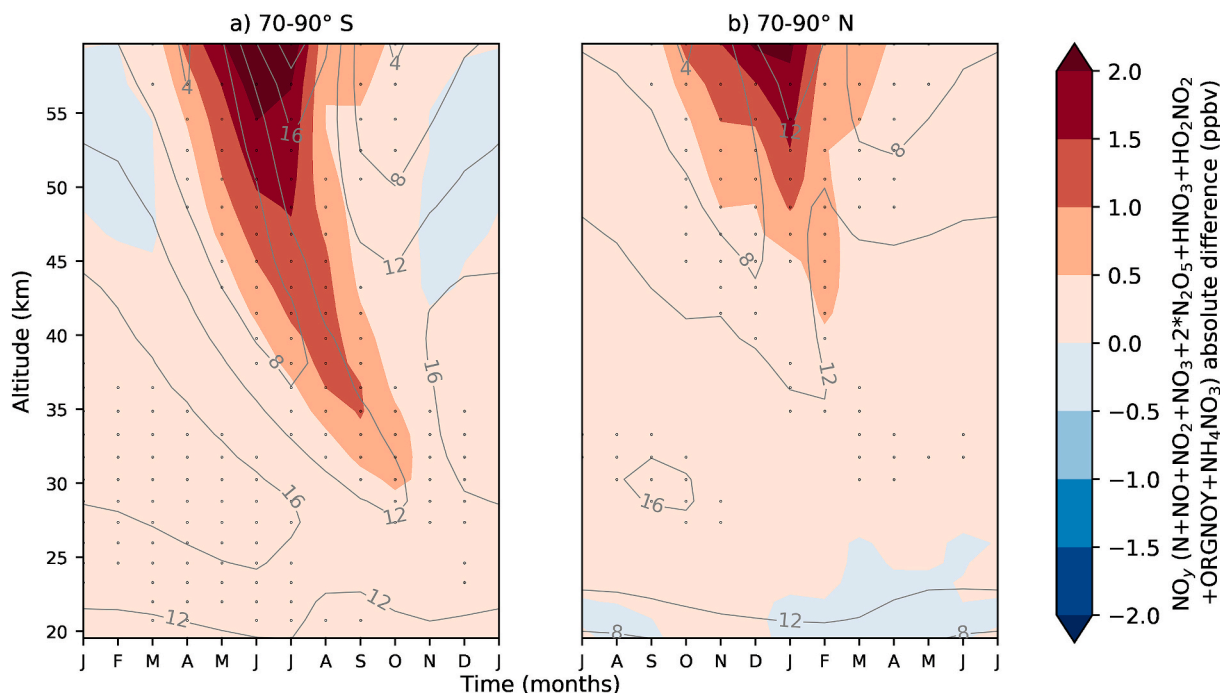|	Ctrl run	MEE exp	MEE-Ctrl (m/s), with/without SSWs
Northern Hemisphere (60°, 50 km)			
December	42	42	2.4/2.9
January	52	50	1.2/1.4
February	42	34	1.2/0.7
March	52	61	1.5/1.6
Southern Hemisphere (60°, 50 km)			
June	0	0	.6/.6
July	0	0	.1/.4
August	0	2	−2.2/−2.1
September	4	17	−1.1/−1.8

Fig. A.1. Climatological annual cycle of the monthly zonal-mean NO_y anomalies (ppbv, in filled contours) and absolute NO_y from the control run (ppbv, gray contours), averaged over latitudes between (a) 70°-90° S and b) 70°-90° N. Black dots represent locations of statistically significant anomalies.
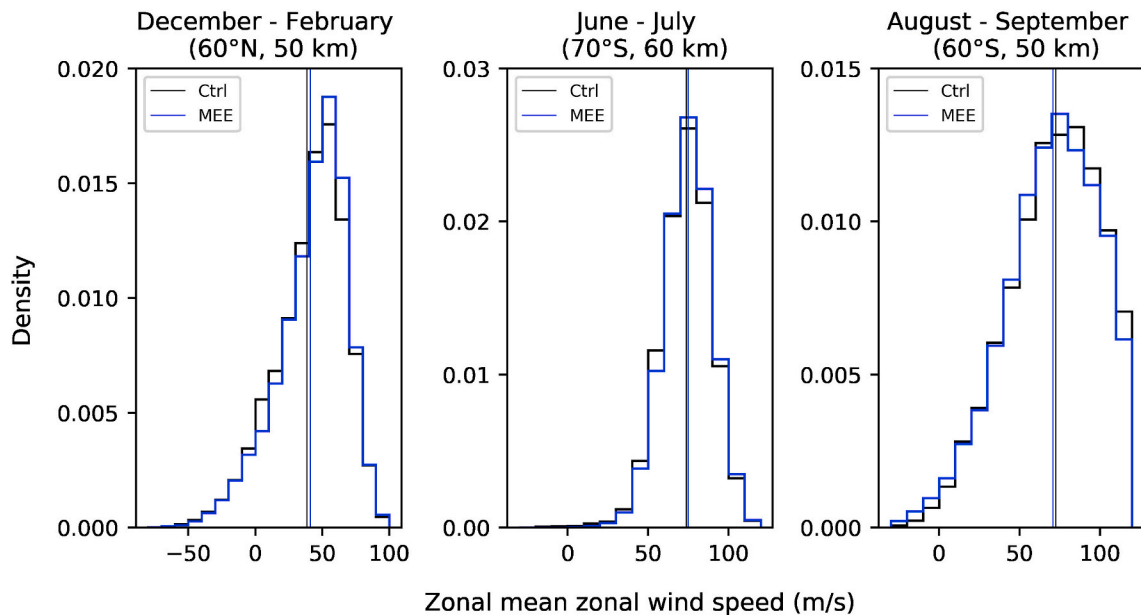

Fig. A.2. Normalized distributions of daily zonal mean zonal winds (ms^{-1}) for the control run (black) and the MEE experiment (blue) and their corresponding time mean (vertical lines) from a) December–February at 60°N at 50 km, b) June–July at 70°S at 60 km and c) August–September at 60°S at 50 km.2
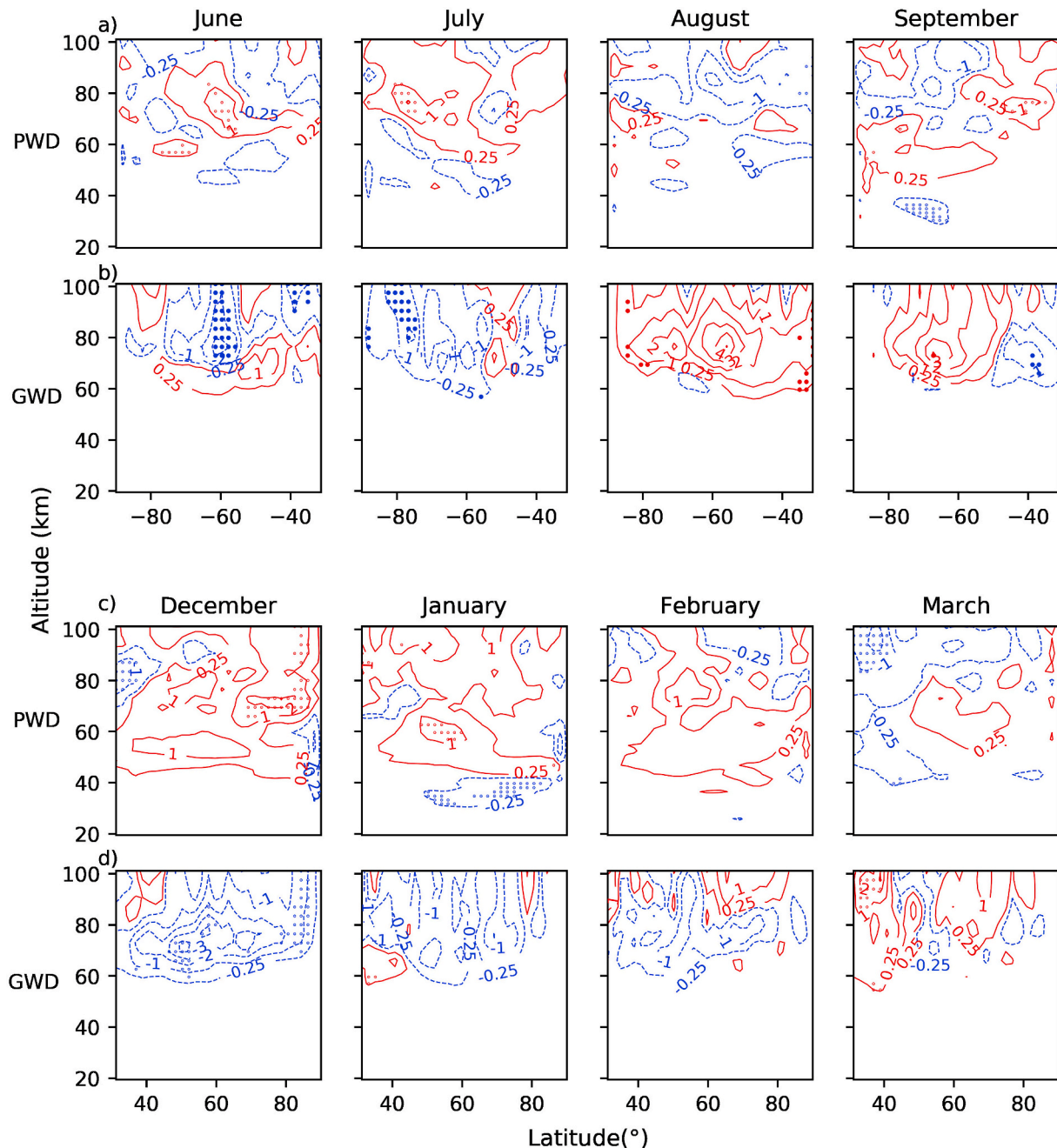
Fig. A.3. The PWD and GWD anomalies ($ms^{-1}day^{-1}$) in (a-b) June–September in SH and (c-d) December–March in NH. Colored dots represent locations of statistically significant PWD and GWD anomalies.

References

Andersson, M.E., Verronen, P.T., Marsh, D.R., Seppälä, A., Päivärinta, S.M., Rodger, C.J., Clilverd, M.A., Kalakoski, N.D., Van De Kamp, M., 2018. Polar ozone response to energetic particle precipitation over decadal time scales: the role of medium-energy electrons. J. Geophys. Res. Atmos. 123, 607–622. https://doi.org/10.1002/2017JD027605.

Andersson, M.E., Verronen, P.T., Rodger, C.J., Clilverd, M.A., Seppälä, A., 2014. Missing driver in the Sun-Earth connection from energetic electron precipitation impacts mesospheric ozone. Nat. Commun. 5, 1–5. https://doi.org/10.1038/ncomms6197.

Andrews, D.G., Holton, J.R., Leovy, C.B., 1987. Middle atmosphere dynamics. Rev. Geophys. https://doi.org/10.1029/RG021i002p00283.

Arsenovic, P., Rozanov, E., Stenke, A., Funke, B., Wissing, J.M., Mursula, K., Tummon, F., Peter, T., 2016. The influence of Middle Range Energy Electrons on atmospheric chemistry and regional climate. J. Atmos. Sol. Terr. Phys. 149, 180–190. https://doi.org/10.1016/j.jastp.2016.04.008.

Baumgaertner, A.J.G., Seppälä, A., Jöckel, P., Clilverd, M.A., 2011. Geomagnetic activity related NOx enhancements and polar surface air temperature variability in a chemistry climate model: modulation of the NAM index. Atmos. Chem. Phys. 11, 4521–4531. https://doi.org/10.5194/acp-11-4521-2011.

Brasseur, G., Solomon, S., 2005. Aeronomy of the Middle Atmosphere: Chemistry and Physics of the Stratosphere and Mesosphere, 3rd revis. Springer, New York.

Callis, L.B., Baker, D.N., Blake, J.B., Lambeth, J.D., Boughner, R.E., Natarajan, M., Klebesadel, R.W., Gorney, D.J., 1991. Precipitating relativistic electrons: their long-term effect on stratospheric odd nitrogen levels. J. Geophys. Res. 96, 2939–2976. https://doi.org/10.1029/90JD02184.

Cullens, C.Y., England, S.L., Garcia, R., 2016. The 11 year solar cycle signature on wave-driven dynamics in WACCM. J. Geophys. Res. Sp. Phys. 121, 3484–3496. https://doi.org/10.1002/2016JA022455.

Damiani, A., Funke, B., López-Puertas, M., Santee, M.L., Cordero, R.R., Watanabe, S., 2016. Energetic particle precipitation: a major driver of the ozone budget in the Antarctic upper stratosphere. Geophys. Res. Lett. https://doi.org/10.1002/2016GL068279.

Funke, B., López-Puertas, M., Stiller, G.P., von Clarmann, T., 2014. Mesospheric and stratospheric NOy produced by energetic particle precipitation during 2002–2012. J. Geophys. Res. https://doi.org/10.1002/2013JD021404.

Fytterer, T., Santee, M.L., Sinnhuber, M., Wang, S., 2015. The 27 day solar rotational effect on mesospheric nighttime OH and O3 observations induced by geomagnetic activity. J. Geophys. Res. A Sp. Phys. https://doi.org/10.1002/2015JA021183.

Gray, L.J., Beer, J., Geller, M., Haigh, J.D., Lockwood, M., Matthes, K., Cubash, U., Fleitmann, D., Harrison, G., Hood, L., Luterbacher, J., Meehl, G.A., Shindell, D., van Geel, B., White, W., 2010. Solar influences on climate. Rev. Geophys. 48, RG4001. https://doi.org/10.1029/2009RG000282.

Jackman, C.H., Fleming, E.L., Vitt, F.M., 2000. Influence of extremely large solar proton events in a changing stratosphere. J. Geophys. Res. Atmos. 105, 11659–11670. https://doi.org/10.1029/2000JD900010.

Jackman, C.H., Marsh, D.R., Vitt, F.M., Garcia, R.R., Randall, C.E., Fleming, E.L., Frith, S. M., 2009. Long-term middle atmospheric influence of very large solar proton events. J. Geophys. Res. Atmos. 114, 1–14. https://doi.org/10.1029/2008JD011415.

Kay, J.E., Deser, C., Phillips, A., Mai, A., Hannay, C., Strand, G., Arblaster, J.M., Bates, S. C., Danabasoglu, G., Edwards, J., Holland, M., Kushner, P., Lamarque, J.F., Lawrence, D., Lindsay, K., Middleton, A., Munoz, E., Neale, R., Oleson, K., Polvani, L., Vertenstein, M., 2015. The community earth system model (CESM) large ensemble project : a community resource for studying climate change in the presence of internal climate variability. Bull. Am. Meteorol. Soc. 96, 1333–1349. https://doi.org/10.1175/BAMS-D-13-00255.1.

Kinnison, D.E., Brasseur, G.P., Walters, S., Garcia, R.R., Marsh, D.R., Sassi, F., Harvey, V. L., Randall, C.E., Emmons, L., Lamarque, J.F., Hess, P., Orlando, J.J., Tie, X.X., Randel, W., Pan, L.L., Gettelman, A., Granier, C., Diehl, T., Niemeier, U., Simmons, A.J., 2007. Sensitivity of chemical tracers to meteorological parameters in the MOZART-3 chemical transport model. J. Geophys. Res. Atmos. https://doi.org/10.1029/2006JD007879.

Kodera, K., Kuroda, Y., 2002. Dynamical response to the solar cycle. J. Geophys. Res. Atmos. 107, 1–12. https://doi.org/10.1029/2002JD002224.

Kvissel, O.K., Orsolini, Y.J., Stordal, F., Isaksen, I.S.A., Santee, M.L., 2012. Formation of stratospheric nitric acid by a hydrated ion cluster reaction: implications for the effect of energetic particle precipitation on the middle atmosphere. J. Geophys. Res. 117, 1–16. https://doi.org/10.1029/2011JD017257.

Lockwood, M., 2012. Solar influence on global and regional climates. Surv. Geophys. 33, 503–534. https://doi.org/10.1007/s10712-012-9181-3.

Marsh, D.R., Garcia, R.R., Kinnison, D.E., Boville, B.A., Sassi, F., Solomon, S.C., Matthes, K., 2007. Modeling the whole atmosphere response to solar cycle changes in radiative and geomagnetic forcing. J. Geophys. Res. Atmos. 112, 1–20. https://doi.org/10.1029/2006JD008306.

Marsh, D.R., Mills, M.J., Kinnison, D.E., Lamarque, J.F., Calvo, N., Polvani, L.M., 2013. Climate change from 1850 to 2005 simulated in CESM1(WACCM). J. Clim. 26, 7372–7391. https://doi.org/10.1175/JCLI-D-12-00558.1.

Matthes, K., Funke, B., Andersson, M.E., Barnard, L., Beer, J., Charbonneau, P., Clilverd, M.A., Dudok De Wit, T., Haberreiter, M., Hendry, A., Jackman, C.H., Kretzschmar, M., Kruschke, T., Kunze, M., Langematz, U., Marsh, D.R., Maycock, A. C., Misios, S., Rodger, C.J., Scaife, A.A., Seppälä, A., Shangguan, M., Sinnhuber, M., Tourpali, K., Usoskin, I., Van De Kamp, M., Verronen, P.T., Versick, S., 2017. Solar forcing for CMIP6 (v3.2). Geosci. Model Dev. https://doi.org/10.5194/gmd-10-2247-2017.

McCormack, J.P., Nathan, T.R., Cordero, E.C., 2011. The effect of zonally asymmetric ozone heating on the Northern Hemisphere winter polar stratosphere. Geophys. Res. Lett. 38, 1–5. https://doi.org/10.1029/2010GL045937.

Meraner, K., Schmidt, H., 2018. Climate impact of idealized winter polar mesospheric and stratospheric ozone losses as caused by energetic particle precipitation. Atmos. Chem. Phys. 18, 1079–1089. https://doi.org/10.5194/acp-18-1079-2018.

Mironova, I.A., Aplin, K.L., Arnold, F., Bazilevskaya, G.A., Harrison, R.G., Krivolutsky, A. A., Nicoll, K.A., Rozanov, E.V., Turunen, E., Usoskin, I.G., 2015. Energetic particle influence on the earth's atmosphere. Space Sci. Rev. https://doi.org/10.1007/s11214-015-0185-4.

Mironova, I.A., Artamonov, A.A., Bazilevskaya, G.A., Rozanov, E.V., Kovaltsov, G.A., Makhmutov, V.S., Mishev, A.L., Karagodin, A.V., 2019. Ionization of the polar atmosphere by energetic electron precipitation retrieved from balloon measurements. Geophys. Res. Lett. 46, 990–996. https://doi.org/10.1029/2018GL079421.

Neale, R.B., Gettelman, A., Park, S., Chen, C., Lauritzen, P.H., Williamson, D.L., Conley, A.J., Kinnison, D., Marsh, D., Smith, A.K., Vitt, F., Garcia, R., Lamarque, J., Mills, M., Tilmes, S., Morrison, H., Cameron-smith, P., Collins, W.D., Iacono, M.J., Easter, R.C., Liu, X., Ghan, S.J., Rasch, P.J., Taylor, M.A., 2012. Description of the NCAR community atmosphere model (CAM5). NCAR Tech. Note TN-486.

Newnham, D.A., Clilverd, M.A., Rodger, C.J., Hendrickx, K., Megner, L., Kavanagh, A.J., Seppälä, A., Verronen, P.T., Andersson, M.E., Marsh, D.R., Kovács, T., Feng, W.,

Plane, J.M.C., 2018. Observations and modeling of increased nitric oxide in the antarctic polar middle atmosphere associated with geomagnetic storm-driven energetic electron precipitation. J. Geophys. Res. Sp. Phys. 123, 6009–6025. https://doi.org/10.1029/2018JA025507.

Newnham, D.A., Espy, P.J., Clilverd, M.A., Rodger, C.J., Seppälä, A., Maxfield, D.J., Hartogh, P., Holmén, K., Horne, R.B., 2011. Direct observations of nitric oxide produced by energetic electron precipitation into the Antarctic middle atmosphere. Geophys. Res. Lett. 38, 1–5. https://doi.org/10.1029/2011GL048666.

Peters, D.H.W., Schneidereit, A., Bügelmayer, M., Zülicke, C., Kirchner, I., 2015. Atmospheric circulation changes in response to an observed stratospheric zonal ozone anomaly. Atmos.-Ocean 53, 74–88. https://doi.org/10.1080/07055900.2013.878833.

Reddmann, T., Ruhnke, R., Versick, S., Kouker, W., 2010. Modeling disturbed stratospheric chemistry during solar-induced NO x enhancements observed with MIPAS/ENVISAT. J. Geophys. Res. https://doi.org/10.1029/2009jd012569.

Richter, J.H., Sassi, F., Garcia, R.R., 2010. Toward a physically based gravity wave source parameterization in a general circulation model. J. Atmos. Sci. 67, 136–156. https://doi.org/10.1175/2009jas3112.1.

Rodger, C.J., Clilverd, M.A., Seäpplä, A., Thomson, N.R., Gamble, R.J., Parrot, M., Sauvaud, J.A., Ulich, T., 2010. Radiation belt electron precipitation due to geomagnetic storms: significance to middle atmosphere ozone chemistry. J. Geophys. Res. Sp. Phys. 115, 1–12. https://doi.org/10.1029/2010JA015599.

Rozanov, E., Calisto, M., Egorova, T., Peter, T., Schmutz, W., 2012. Influence of the precipitating energetic particles on atmospheric chemistry and climate. Surv. Geophys. 33, 483–501. https://doi.org/10.1007/s10712-012-9192-0.

Rozanov, E., Callis, L., Schlesinger, M., Yang, F., Andronova, N., Zubov, V., 2005. Atmospheric response to NOy source due to energetic electron precipitation. Geophys. Res. Lett. https://doi.org/10.1029/2005GL023041.

Semeniuk, K., Fomichev, V.I., McConnell, J.C., Fu, C., Melo, S.M.L., Usoskin, I.G., 2011. Middle atmosphere response to the solar cycle in irradiance and ionizing particle precipitation. Atmos. Chem. Phys. 11, 5045–5077. https://doi.org/10.5194/acp-11-5045-2011.

Seppälä, A., Lu, H., Clilverd, M.A., Rodger, C.J., 2013. Geomagnetic activity signatures in wintertime stratosphere wind, temperature, and wave response. J. Geophys. Res. Atmos. 118, 2169–2183. https://doi.org/10.1002/jgrd.50236.

Seppälä, A., Randall, C.E., Clilverd, M.A., Rozanov, E., Rodger, C.J., 2009. Geomagnetic activity and polar surface air temperature variability. J. Geophys. Res. Sp. Phys. 114, 1–10. https://doi.org/10.1029/2008JA014029.

Sinnhuber, M., Berger, U., Funke, B., Nieder, H., Reddmann, T., Stiller, G., Versick, S., Von Clarmann, T., Wissing, J.M., 2018. NOy production, ozone loss and changes in net radiative heating due to energetic particle precipitation in 2002-2010. Atmos. Chem. Phys. 18, 1115–1147. https://doi.org/10.5194/acp-18-1115-2018.

Sinnhuber, M., Funke, B., 2020. Energetic electron precipitation into the atmosphere. In: Jaynes, A., Usanova, M. (Eds.), The Dynamic Loss of Earth's Radiation Belts. Elsevier, Amsterdam, pp. 279–321. https://doi.org/10.1016/B978-0-12-813371-2.00009-3.

Smith-Johnsen, C., Marsh, D.R., Orsolini, Y., Nesse Tyssøy, H., Hendrickx, K., Sandanger, M.I., Ødegaard, L.K.G., Stordal, F., 2018. Nitric oxide response to the april 2010 electron precipitation event: using WACCM and WACCM-D with and without medium-energy electrons. J. Geophys. Res. Sp. Phys. 123, 5232–5245. https://doi.org/10.1029/2018JA025418.

Tomikawa, Y., 2017. Response of the middle atmosphere in the southern hemisphere to energetic particle precipitation in the latest reanalysis data. Sola 13A, 1–7. https://doi.org/10.2151/sola.13A-001.

Tyssøy, H.N., Haderlein, A., Sandanger, M.I., Stadsnes, J., 2019. Intercomparison of the POES/MEPED loss cone electron fluxes with the CMIP6 parametrization. J. Geophys. Res. Sp. Phys. https://doi.org/10.1029/2018JA025745.

Van De Kamp, M., Seppälä, A., Clilverd, M.A., Rodger, C.J., Verronen, P.T., Whittaker, I. C., 2016. A model providing long-term data sets of energetic electron precipitation during geomagnetic storms. J. Geophys. Res. 121, 520–540. https://doi.org/10.1002/2015JD024212.

van Loon, H., 2012. Why is the influence of sunspot peaks on the ocean and atmosphere in northern winter seen mainly in the pacific region?, 2012 ISRN Meteorol 1–5. https://doi.org/10.5402/2012/427457.

Waugh, D.W., Oman, L., Newman, P.A., Stolarski, R.S., Pawson, S., Nielsen, J.E., Perlwitz, J., 2009. Effect of zonal asymmetries in stratospheric ozone on simulated Southern Hemisphere climate trends. Geophys. Res. Lett. 36, 1–6. https://doi.org/10.1029/2009GL040419.

Zhang, Y., Paxton, L.J., 2008. An empirical Kp-dependent global auroral model based on TIMED/GUVI FUV data. J. Atmos. Sol. Terr. Phys. 70, 1231–1242. https://doi.org/10.1016/j.jastp.2008.03.008.